Computers and Structures 177 (2016) 69–82

Contents lists available at ScienceDirect

Computers and Structures

journal homepage: www.elsevier.com/locate/compstruc

A four-node quadrilateral element fitted to numerical manifold method with continuous nodal stress for crack analysis

Yongtao Yang [a], Guanhua Sun [a,*], Hong Zheng [b], Xiaodong Fu [a]

[a] State Key Laboratory of Geomechanics and Geotechnical Engineering, Institute of Rock and Soil Mechanics, Chinese Academy of Sciences, Wuhan 430071, China
[b] Key Laboratory of Urban Security and Disaster Engineering, Ministry of Education, Beijing University of Technology, Beijing 100124, China

ARTICLE INFO

Article history:
Received 30 July 2016
Accepted 15 August 2016

Keywords:
Numerical manifold method
Quad4-CNS(NMM) element
Stress intensity factor
Crack propagation
Continuous nodal stress

ABSTRACT

Formulations of a four-node quadrilateral element fitted to numerical manifold method (NMM) with continuous nodal stress called Quad4-CNS (NMM) element for two-dimensional (2D) crack analysis are presented. This Quad4-CNS (NMM) element can be considered as a development of the recently published four-node quadrilateral element with continuous nodal stress (Quad4-CNS). In contrast to the four-node iso-parametric quadrilateral element (Quad4), the Quad4-CNS element has higher order of global approximations, much better accuracy and continuous nodal stress. Moreover, it is free from the "linear dependence" which otherwise cripples many of the partition of unity (PU) based methods with high order global approximations. Due to the adoption of two cover systems, namely, the mathematical cover and physical cover, the NMM is capable of solving continuous and discontinuous problems in a unified way. The purpose of this paper is to synergize the advantages of both the Quad4-CNS element and the NMM to precisely model linear elastic fracture problems. A number of numerical examples indicate the accuracy and robustness of the present Quad4-CNS (NMM) element.

1. Introduction

The modeling of complex crack problems to predict the life span of cracked structures is still full of challenges and difficulties. Over the past several decades, many numerical approaches have been proposed to fulfill this task. The finite element method (FEM) [1], as a representative, has been used to solve a great number of crack problems [2,3]. The FEM, however, has to deploy a mesh which should conform to the crack faces to simulate cracked bodies. This will lead to a great burden in meshing and remeshing for complex crack propagation problems [4]. In order to alleviate the burden of tip-remeshing, the algorithm of edge rotation has been proposed in the framework of FEM, see details in [5–7].

Alternatively, meshfree methods only employ nodes to descretize the problem domain and therefore are immunized from mesh related problems, and are very suitable to solve crack propagation problems [8,9]. Some important work related to meshfree methods can be found in [10–16]. Like FEM, meshfree methods also suffer from drawbacks, such as essential boundary condition implementation handicap, high computational cost and complex process in constructing the trial functions [17]. As a result, some hybrid schemes [18,19] have been proposed to improve the property of meshfree methods.

To mitigate the burden of meshing and remeshing in modeling crack problems, the extended finite element method (XFEM) [20] which is considered as an improvement of FEM has been developed. XFEM is based on the partition of unity method (PUM) [21], where the representation of a strong or weak discontinuity is achieved via enrichment of the shape functions [22]. In order to synergize the advantages of both the extended FEM and isogeometric analysis (IGA), the extended isogeometric (XIGA) [23] have been proposed. Up to now, XFEM and XIGA have been successfully used to solve many complex problems such as holes and inclusions [24], cracks in multiphase composites [25–29], functionally graded materials (FGMs) [30–34] and quasi-brittle concrete structures [35].

Like XFEM, the numerical manifold method (NMM) [36] can also be considered as an improvement of FEM. Due to the adoption of mathematical cover and physical cover, NMM is capable of simulating continuous and discontinuous problems in a unified way. In NMM, the mathematical cover is utilized to define the PU functions. The physical cover, generated by cutting the mathematical cover with the problem domain, is used to define the local approximations. In this way, NMM can capture discontinuity in a nature way without recourse to other enrichment function such as the generalized Heaviside function. Besides, NMM can deploy

* Corresponding author.
E-mail address: ghsun@whrsm.ac.cn (G. Sun).

http://dx.doi.org/10.1016/j.compstruc.2016.08.008
0045-7949/

mathematical mesh without considering the features of the problem domain which indicates that NMM can avoid remeshing for crack propagation problems. In addition, NMM is the generalization of the discontinuous deformation analysis (DDA) [37–39] that addresses the system of distinct rock blocks. Since the advent, NMM has been successfully used to model static crack problems [40–42], dynamic crack problems [43], Kirchhoff's thin plate bending problems [44], and seepage problems [45–46].

It is well-known that the stress field by means of FEM with standard DOFs is discontinuous among internal element edges and nodes, such as the three-node triangular element (Trig3) and the four-node iso-parametric quadrilateral element (Quad4). Extra smoothing operations are required to calculate nodal stress in the post processing. Besides, accuracy of some classic iso-parametric elements is highly sensitive to the quality of meshes [47]. To improve the property of Quad4 element, Tang et al. [48] developed a partition-of-unity-based four-node quadrilateral element with continuous nodal stress (Quad4-CNS). By increasing the order of global approximation functions, Quad4-CNS element obtains better accuracy, higher convergence rate and higher tolerance to mesh distortion as compared to the Quad4 element. Moreover, it is free from the "linear dependence" issue which otherwise cripples many of the PU based methods. Notice that Quad4-CNS element does not alter the total number of the degrees of freedom (DOFs) of the whole system. It implies that the total number of DOFs generated by the use of Quad4-CNS element is the same as that by the standard Quad4 element. In another front, Bui et al. [49] also formulated a new four-node quadrilateral element with continuous nodal stress and applied this element to linear elastic fracture mechanics [50]. However, the element developed by Tang et al. [48] and the element developed by Bui et al. [49] are totally different. The element developed by Tang et al. is a development of the 'FE-Meshfree' QUAD4 element with least square point interpolation functions (Quad4-LSPIM) [51], while the element by Bui et al. is based on the twice-interpolation procedure presented in [17,52].

In order to synergize the advantages of both the Quad4-CNS element and the numerical manifold method (NMM), a four-node quadrilateral element fitted to the numerical manifold method with continuous nodal stress (Quad4-CNS (NMM)) for linear elastic fracture problems is developed in this study. The property and performance of the present Quad4-CNS (NMM) element will be studied in great detail in the rest of this paper. The outline of this paper is as follows: Section 2 briefly introduces the numerical manifold method (NMM); Section 3 presents the formulation of Quad4-CNS (NMM) element for crack problem in 2D elastic solids in detail; The interaction integral and the SIFs calculation are described in Section 4. The numerical examples and discussions are subsequently presented in Section 5. Some conclusions are drawn in the last section.

2. Review on NMM

There are three important concepts in NMM, namely, the mathematical cover (MC), the physical cover (PC) and the manifold element (ME) [53]. The mathematical cover is the union of user-defined overlapping small domains. Each small domain (Ω_i^m) is called mathematical patch (MP). The mathematical cover can be deployed as the user wishes, but must cover the physical domain of the problem. By cutting the mathematical patches one after another with the components of the problem domain, including the domain boundaries, the material interfaces, and the discontinuities, the physical patches (PPs) are generated. The union of all the physical patches is called the physical cover (PC) which will exactly cover the whole problem domain (Ω). The manifold element in NMM is defined as the common region of several PPs. manifold elements are the basic units for integrating the weak form of the problem.

Shown in Fig. 1 is an example used to explain the above mentioned concepts. The regular quadrilateral mesh forms the mathematical cover, while the red lines define problem domain (Ω). In theory, mathematical cover can be formed arbitrarily [53]. However, for the simplicity of implementation, almost all application and development of NMM have been selecting finite element meshes to construct the mathematical cover. The regular mesh used here is called mathematical mesh. The mathematical mesh does not have to match the boundary or crack face of, but must cover the problem domain. The rectangle with yellow edges denotes a mathematical patch Ω_i^m and the circular red dot named as a star represents the center of corresponding mathematical patch.

Cutting Ω_9^m with problem domain components yields two physical patches, namely, Ω_{1-9}^p and Ω_{2-9}^p. Cutting Ω_8^m with problem domain components yields only one physical patch, namely, Ω_{1-8}^p, which coincides with Ω_8^m. Cutting mathematical patch Ω_{10}^m with problem domain components, only the fraction inside the problem domain forms a physical patch, namely, Ω_{1-10}^p, but the rest part of Ω_{10}^m will be discarded.

Each physical patch has and only has a corresponding node called "generalized node" which is equivalent to the node in FEM. However, the "generalized node" in NMM has its own character. The degree of freedoms for each physical patch is defined on the generalized node. It can be seen in Fig. 1 that the generalized node of physical patch Ω_{1-8}^p, denoted as GN_{1-8}^p is the center of physical patch Ω_{1-8}^p. The generalized node of physical patch Ω_{1-1}^p, denoted as GN_{1-1}^p, however, is outside of Ω_{1-1}^p domain. The generalized nodes of physical patches Ω_{1-9}^p and Ω_{2-9}^p coincide with each other. It can be seen that the generalized nodes in Fig. 1 are deployed regularly without considering the influence of problem

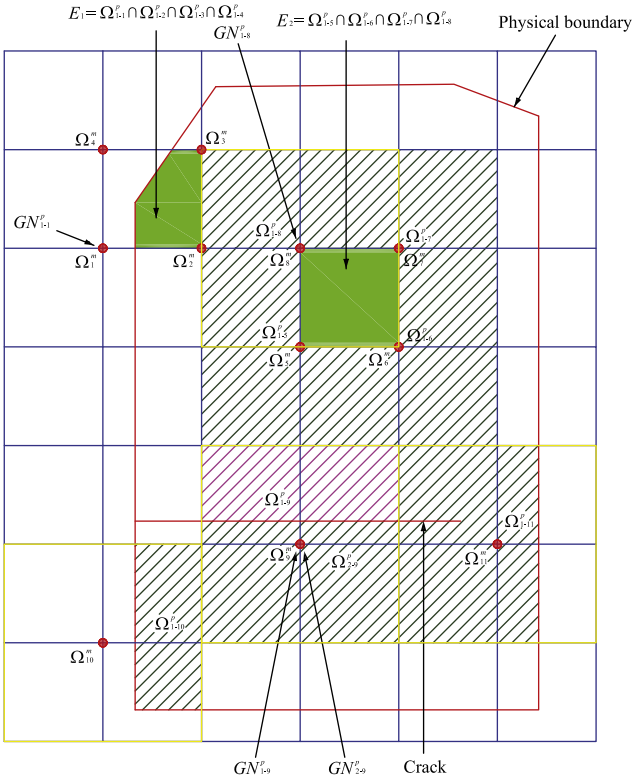

Fig. 1. Mathematical patches, physical patches and manifold elements in NMM.

domain components. For the simplicity of description, the "generalized node" in NMM will also be termed as "node" in the rest of this study.

Two types of physical patches [53], namely, nonsingular patches and singular patches are used in this study. The nonsingular patches do not contain any crack tip in their corresponding domains, like Ω^p_{1-8} and Ω^p_{1-10}, while the singular patches contain at least one crack tip in their corresponding domains, like Ω^p_{1-11}, as shown in Fig. 1.

The common domains of physical patches will produce different manifold elements E_i, $i = 1,\ldots nm$. Here, nm is the number of manifold elements in the problem domain. Intersecting physical patches Ω^p_{1-1}, Ω^p_{1-2}, Ω^p_{1-3} and Ω^p_{1-4} will produce manifold element $E_1 = \Omega^p_{1-1} \cap \Omega^p_{1-2} \cap \Omega^p_{1-3} \cap \Omega^p_{1-4}$, while intersecting physical patches Ω^p_{1-5}, Ω^p_{1-6}, Ω^p_{1-7} and Ω^p_{1-8} will produce manifold element $E_2 = \Omega^p_{1-5} \cap \Omega^p_{1-6} \cap \Omega^p_{1-7} \cap \Omega^p_{1-8}$. A manifold element in NMM can be in arbitrary shape: the shape of E_2 is a quadrangle, but the shape of E_1 is a pentagon. Furthermore, the manifold elements in this study are classified into three types, namely, (1) normal manifold element covered only by nonsingular patches; (2) blending manifold element covered by both singular patches and nonsingular patches; (3) singular manifold element covered only by singular patches.

Over each mathematical patch, Ω^m_i, a weight function (or PU function) $w_i(\boldsymbol{x})$ can be defined, which satisfies

$$w_i(\boldsymbol{x}) = 0, \quad \text{if } \boldsymbol{x} \notin \Omega^m_i, \tag{1.1}$$

$$0 \leqslant w_i(\boldsymbol{x}) \leqslant 1, \quad \text{if } \boldsymbol{x} \in \Omega^m_i, \tag{1.2}$$

$$\sum_{i=1}^{n^m} w_i(\boldsymbol{x}) = 1, \quad \text{if } \boldsymbol{x} \in \Omega \tag{1.3}$$

The weight function $w_i(\boldsymbol{x})$ associated with Ω^m_i will be accordingly transferred to Ω^p_{j-i}, and denoted as $w_{j-i}(\boldsymbol{x})$. For the simplicity of presentation, all the physical patch Ω^p_{j-i} and weight function $w_{j-i}(\boldsymbol{x})$ are coded with a single subscript and denoted as Ω^p_k and $w_k(\boldsymbol{x})$, respectively. Over each physical patch Ω^p_k, different local approximation functions (also named as cover function) $u_k(\boldsymbol{x})$ will be defined. This enables NMM to simulate discontinuity across the common boundaries between different physical patches.

Over each physical patch Ω^p_k, the local approximation function $u_k(\boldsymbol{x})$ which reflects the known information about the boundary value problem or the input data to model problems can be defined. In this study, the polynomial approximation functions are adopted over the nonsingular patches, while the asymptotic crack-tip functions capable of capturing the singular field around the crack tip are adopted over the singular patches.

The local approximation function $u_k(\boldsymbol{x})$ of order n for a nonsingular patch can be defined as

$$u_k(\boldsymbol{x}) = \boldsymbol{p}(\boldsymbol{x})^T \boldsymbol{d}_k \tag{2}$$

where $\boldsymbol{d_k}$ is an array of unknown coefficients, and $\boldsymbol{p}(\boldsymbol{x})$ is the matrix of polynomial bases. If the number of polynomial terms m is chosen to be one, three or six, then the polynomial bases $\boldsymbol{p}(\boldsymbol{x})$ is expressed as $\boldsymbol{p}(\boldsymbol{x}) = \{1\}^T$ $(n = 0)$, $\boldsymbol{p}(\boldsymbol{x}) = \{1\ x\ y\}^T$ $(n = 1)$ or $\boldsymbol{p}(\boldsymbol{x}) = \{1\ x\ y\ xy\ xx\ yy\}^T$ $(n = 2)$, respectively.

The local approximation function $u_k(\boldsymbol{x})$ for a singular patch, can be constructed by adding the polynomial function with the asymptotic crack-tip functions, and expressed as

$$u_k(\boldsymbol{x}) = \boldsymbol{p}(\boldsymbol{x})^T \boldsymbol{d}_k + \boldsymbol{F}^e(\boldsymbol{x})^T \boldsymbol{e}_k \tag{3}$$

where $\boldsymbol{e}_k$ is an array of unknown coefficients, and $\boldsymbol{F}^e(\boldsymbol{x})$ is the first item of Williams' displacement series [54] near the crack tip and defined as

$$\begin{aligned}\boldsymbol{F}^e(\boldsymbol{x}) &= [\,\Psi_1 \quad \Psi_2 \quad \Psi_3 \quad \Psi_4\,]^T \\ &= [\,\sqrt{r}\cos\tfrac{\theta}{2} \quad \sqrt{r}\sin\tfrac{\theta}{2} \quad \sqrt{r}\cos\tfrac{3\theta}{2} \quad \sqrt{r}\cos\tfrac{3\theta}{2}\,]^T\end{aligned} \tag{4}$$

in which $(r,\ \theta)$ is the polar coordinates with regard to the polar system defined at the crack tip. Note that the latter two basic functions, Ψ_3 and Ψ_4, are different from the literature, where $\Psi_3 = \sqrt{r}\sin\theta\sin\frac{\theta}{2}$ and $\Psi_4 = \sqrt{r}\sin\theta\cos\frac{\theta}{2}$. The two forms of bases obviously span the same subspace and make no difference. As discussed in [53], the purpose to take the form presented in Eq. (4) is to simplify the implementation if more enriched terms should be considered.

After defining the weight functions and the local approximations, the global approximation on a given manifold element is approximated to be

$$u^h(\boldsymbol{x}) = \sum_{k=1}^{n^{pj}} w_k(\boldsymbol{x}) u_k(\boldsymbol{x}) \tag{5}$$

where n^{pj} denotes the number of physical patches for a manifold element E_j.

It can be seen in Eq. (5) that NMM could construct high order global approximation of any order by simply increasing the order of weight functions and local approximations and obtain better accuracy of the solution to the problem. Using directly the high order $(n \geqslant 1)$ polynomial approximation functions presented in Eq. (2), however, as in GFEM, will significantly increase the number of global DOFs. Moreover, this will arise the LD problem. Some effective approaches have been suggested in the context of GFEM and NMM to deal with the LD problem [53,55–57].

3. Formulation for Quad4-CNS(NMM)

As can be seen in [48,58], Quad4-CNS element can obtain better accuracy, higher convergence rate and higher tolerance to mesh distortion than the four-node quadrilateral element (Quad4) for linear elastic and vibration problems by simply using the same mesh as in Quad4 element. However, Quad4-CNS element adopts quadrilateral mesh which should conform to the boundary of problem domain to construct its shape functions. As in FEM, the issue related to meshing and remeshing also exists in Quad4-CNS element for crack propagation problems, although commercial software is able to generate high quality quadrilateral mesh for problems with simple geometric boundary. Since mathematical mesh in NMM needs not to conform to the crack faces, crack analysis by NMM should be very convenient. In view of the advantages of both Quad4-CNS element and NMM, formulation of a four-node quadrilateral element fitted to the numerical manifold method with continuous nodal stress (Quad4-CNS (NMM)) is present in detail in this section.

Based on the concept of NMM, the global approximation of Quad4-CNS (NMM) element can be expressed as:

$$u^h(\boldsymbol{x}) = w_1(\boldsymbol{x})u_1(\boldsymbol{x}) + w_2(\boldsymbol{x})u_2(\boldsymbol{x}) + w_3(\boldsymbol{x})u_3(\boldsymbol{x}) + w_4(\boldsymbol{x})u_4(\boldsymbol{x}) \tag{6}$$

where $w_i(\boldsymbol{x})$ and $u_i(\boldsymbol{x})$ are the weight function and the local approximation function associated with physical patch Ω^p_i, respectively.

3.1. Weight functions of Quad4-CNS (NMM)

The weight functions $\{w_i(\boldsymbol{x}),\ i = 1,2,3,4\}$ with the global Cartesian coordinates are mapped from 'parent' weight functions in the local coordinates [48]. The formulations for coordinate transformation are represented as:

$$x = \widetilde{\mathrm{N}}_1(\xi,\eta)x_1 + \widetilde{\mathrm{N}}_2(\xi,\eta)x_2 + \widetilde{\mathrm{N}}_3(\xi,\eta)x_3 + \widetilde{\mathrm{N}}_4(\xi,\eta)x_4 \tag{7}$$

$$y = \widetilde{\mathrm{N}}_1(\xi,\eta)y_1 + \widetilde{\mathrm{N}}_2(\xi,\eta)y_2 + \widetilde{\mathrm{N}}_3(\xi,\eta)y_3 + \widetilde{\mathrm{N}}_4(\xi,\eta)y_4 \tag{8}$$

where $\widetilde{\mathrm{N}}_1(\xi,\eta),\ \widetilde{\mathrm{N}}_2(\xi,\eta),\ \widetilde{\mathrm{N}}_3(\xi,\eta),\ \widetilde{\mathrm{N}}_4(\xi,\eta)$ are expressed in the following form [1]

$$\widetilde{\mathrm{N}}_i(\xi,\eta) = (1+\xi_0)(1+\eta_0)/4,\ \xi_0 = \xi_i\xi,\ \eta_0 = \eta_i\eta,\quad i = 1,2,3,4. \tag{9}$$

Unlike the Quad4-LSPIM element [51], which uses the shape functions of Quad4 element to construct weight functions, the weight functions of Quad4-CNS element are written as [48]

$$w_i(\xi,\eta) = (1+\xi_0)(1+\eta_0)(2+\xi_0+\eta_0-\xi^2-\eta^2)/8,\quad i = 1,2,3,4. \tag{10}$$

As discuss in [48], there are three important features for the weight functions of Quad4-CNS (NMM) element, namely, (i) they satisfy the PU condition: $\sum_{i=1}^{4} w_i(\xi,\eta) = 1$, (ii) the weight functions satisfy the Kronecker-delta property $w_i(\boldsymbol{x}_j) = \delta_{ij}$ (i, j = 1,2,3,4), (iii) Moreover, the gradient of the weight functions is continuous at all the nodes, which is the best property that Quad4-LSPIM element does not have.

3.2. Local approximation of Quad4-CNS (NMM)

Explicit polynomials (Eq. (2)) are adopted to construct the local approximations of standard NMM. In other front, 'FE-Meshfree' elements [59,60] use the meshfree shape functions to construct the local approximations without increasing the number of global DOFs and inducing the LD problem. Several methods which possess the desired Kronecker-delta property have been proposed to construct the local approximations of 'FE-Meshfree' elements such as LSPIM [59], reduced CO-MLS (CO-LS) [61] and radial-polynomial basis functions [62]. Here, the constrained and orthonormalized least-squares method (CO-LS) (see details in [48]), which is constrained at its central node, is briefly introduced and used to construct the local approximations of Quad4-CNS(NMM) element.

In Quad4-CNS (NMM) element, the local approximation $u_i(\boldsymbol{x})$ for physical patch Ω_i^p is constructed by using least-squares method and represented as:

$$u_i(\boldsymbol{x}) = \boldsymbol{p}^{\mathrm{T}}(\boldsymbol{x})\boldsymbol{A}^{-1}\boldsymbol{B}\boldsymbol{a},\quad \boldsymbol{a} = [a_1\ a_2\ \cdots\ a_{n^{[i]}}]^{\mathrm{T}}, \tag{11}$$

The moment matrix $\boldsymbol{A}$ and the basis matrix $\boldsymbol{B}$ are expressed as:

$$\boldsymbol{A} = \sum_{j=1}^{n^{[i]}} \boldsymbol{p}(\boldsymbol{x}_j)\boldsymbol{p}^T(\boldsymbol{x}_j),\quad \boldsymbol{B} = [\boldsymbol{p}(\boldsymbol{x}_1)\quad \boldsymbol{p}(\boldsymbol{x}_2)\cdots\boldsymbol{p}(\boldsymbol{x}_{n^{[i]}})]. \tag{12}$$

in which $n^{[i]}$ represents the number of support nodes for physical patch Ω_i^p, $\boldsymbol{a}$ is a vector of nodal displacements and $\boldsymbol{p}(\boldsymbol{x})$ is a vector of monomials. The choice of $\boldsymbol{p}(\boldsymbol{x})$ will affect the performance of the element. In the present work, the number of polynomial basis terms m is selected as follows [59]: if $5 \geqslant n^{[i]} \geqslant 4$, $m = 4$, the basis function $\boldsymbol{p}(\boldsymbol{x}) = \{1\ x\ y\ xy\}$ will be used; if $7 \geqslant n^{[i]} \geqslant 6$, $m = 6$, the basis function $\boldsymbol{p}(\boldsymbol{x}) = \{1\ x\ y\ xy\ x^2\ y^2\}$ will be used; if $n^{[i]} \geqslant 8$, $m = 8$, the basis function $\boldsymbol{p}(\boldsymbol{x}) = \{1\ x\ y\ xy\ x^2\ y^2\ x^2y\ xy^2\}$ will be used.

In order to improve the property of least-squares method, the constrained and orthonormalized least-squares method (CO-LS) is used based on the Gram-Schmidt orthonormalization process [63]. The vector $\boldsymbol{p}$ can be orthogonalized as:

$$\boldsymbol{s} = [s_1\ s_2\ \cdots\ s_m]^T = \boldsymbol{R}\boldsymbol{p}, \tag{13}$$

$\boldsymbol{R}$ is an orthogonalizing matrix with dimension $m \times m$ and m as the number of the monomial terms of $\boldsymbol{p}(\boldsymbol{x})$. The formula of $\boldsymbol{R}$ is presented in reference [64].

Normalizing vector $\boldsymbol{s}$ yields

$$\boldsymbol{r} = \boldsymbol{H}\boldsymbol{p}, \tag{14}$$

$\boldsymbol{H}$ is an orthonormalizing matrix with dimension $m \times m$ [64].

Using Lagrange multiplier method, the constrained local approximation $u_i(\boldsymbol{x})$ can be constructed as

$$u_i(\boldsymbol{x}) = \sum_{j=1}^{n^{[i]}} \hat{\phi}_j^{[i]}(\boldsymbol{x})a_j, \tag{15}$$

$$\hat{\boldsymbol{\Phi}} = \left[\hat{\phi}_1^{[i]}(\boldsymbol{x})\ \hat{\phi}_2^{[i]}(\boldsymbol{x})\cdots\hat{\phi}_{n^{[i]}}^{[i]}(\boldsymbol{x})\right]^{\mathrm{T}} = \boldsymbol{r}^{\mathrm{T}}(\boldsymbol{x})\boldsymbol{B}^{[i]}, \tag{16}$$

$$\boldsymbol{B}^{[i]} = \left[\boldsymbol{B}_1^{[i]}(\boldsymbol{x})\ \boldsymbol{B}_2^{[i]}(\boldsymbol{x})\cdots\boldsymbol{B}_{n^{[i]}}^{[i]}(\boldsymbol{x})\right], \tag{17}$$

$$\boldsymbol{B}_k^{[i]} = \boldsymbol{r}(\boldsymbol{x}_k) - f_k^{[i]}\boldsymbol{r}(\boldsymbol{x}_i)\quad (k = 1,2,\ldots,n^{[i]}), \tag{18}$$

$$f_k^{[i]} = \begin{cases} \sum_{j=1}^{m}(r_{ji}r_{jk}) \Big/ \sum_{j=1}^{m} R_{ji}^2 & (k \neq i), \\ \left[\sum_{j=1}^{m}(r_{ji}r_{jk}) - 1\right] \Big/ \sum_{j=1}^{m} r_{ji}^2 & (k = i), \end{cases} \quad k = 1,2,\ldots,n^{[i]}. \tag{19}$$

in which $\hat{\phi}_j^{[i]}(\boldsymbol{x})$ is the shape function of the local approximation $u_i(\boldsymbol{x})$ associated with node j.

In defining the support of a given physical patch, the *first order nodal connectivity* which includes the nodes of all the quadrilateral meshes connected to the generalized node of the given physical patch is usually considered. Such a support is called *first order support*. However, if both the physical patch within the computational domain and the physical patch on the computational boundary all adopt the *first order support* to construct the local approximations, the physical patch on the computational boundary may has less support nodes than the physical patch within the computational domain. For this reason, the support of a physical patch in the present Quad4-CNS (NMM) element is determined under the following principles:

(i) For the physical patch within the computational domain, the *first order support* is used to obtain its support nodes.
(ii) For the physical patch on the computational boundary, *first order support* or *second order support* is used to obtain its support nodes, and their effects on the element performance will be studied Section 5.2.

3.3. Shape function of Quad4-CNS (NMM) element

The Quad4-CNS (NMM) global approximation $u^h(\boldsymbol{x})$ can be represented in a common form:

$$u^h(\boldsymbol{x}) = \sum_{k=1}^{N} \phi_k(\boldsymbol{x})a_k, \tag{20}$$

in which $\phi_k(\boldsymbol{x})$ is the shape function corresponding to physical patch Ω_k^p or node k. N is the total number of support nodes for a given point and defined as $N = \sum_{i=1}^{4} n^{[i]}$.

Substitution of Eq. (15) into Eq. (6), and then the Quad4-CNS (NMM) global approximation can be constructed as

$$u^h(\boldsymbol{x}) = \sum_{i=1}^{4} w_i(\boldsymbol{x}) \sum_{j=1}^{n^{[i]}} \Phi_j^{[i]}(\boldsymbol{x})a_j. \tag{21}$$

Recalling that $n^{[i]}$ is the number of support nodes to construct local approximation function $u_i(\boldsymbol{x})$. By manipulating Eq. (21), the

Quad4-CNS (NMM) shape functions in Eq. (20) can be represented as

$$\phi_i(\boldsymbol{x}) = \sum_{j=1}^{4} w_j(\boldsymbol{x}) \Phi_i^{[j]}(\boldsymbol{x}) \tag{22}$$

3.4. Properties of Quad4-CNS (NMM) shape function

Some useful properties of Quad4-CNS (NMM) are shown as follows [48]:

(i) The derivative of weight function is of zero value at the nodes.
(ii) The derivative of Quad4-CNS (NMM) global approximation is continuous at the nodes.
(iii) The Kronecker-delta property.

$$\phi_i(\boldsymbol{x}_j) = \delta_{ij}. \tag{23}$$

3.5. Extended Quad4-CNS (NMM) approximations for cracks

As discussed in [42], NMM could model discontinuities in a natural manner, even for a complex case, without recourse to any enrichment functions, such as Heaviside function widely used in XFEM. However, the asymptotic crack-tip functions introduced in Section 2 is needed to enrich the local approximation of NMM, so as to capture the singularity around the crack tip. The enriched displacement approximation using Quad4-CNS (NMM) element could be obtained in a similar NMM setting, and expressed as

$$u^h(\boldsymbol{x}) = \sum_{i\in I^N} w_i(\boldsymbol{x}) u_i(\boldsymbol{x}) + \sum_{i\in I^S} w_i(\boldsymbol{x}) \sum_{j=1}^{4} \Psi_j(\boldsymbol{x}) e_j \tag{24}$$

where I^S is the set of singular physical patches, and I^N is the set of all the physical patches.

In order to get the interpolation property at nodes, the above formula could be further expressed as

$$u^h(\boldsymbol{x}) = \sum_{i\in I^N} w_i(\boldsymbol{x}) u_i(\boldsymbol{x}) + \sum_{i\in I^S} w_i(\boldsymbol{x}) \left(\sum_{j=1}^{4} (\Psi_j(\boldsymbol{x}) - \Psi_j(\boldsymbol{x}_i)) e_j^i \right). \tag{25}$$

3.6. Discrete equations for Quad4-CNS (NMM) and integration strategies

In Quad4-CNS (NMM) element, mathematical cover does not have to match the boundary of the problem domain, so the displacement boundary conditions cannot be imposed directly as in FEM. The displacement boundary conditions should be included into the potential energy by the Lagrange multiplier method or the penalty function method. In this study, the penalty function method is adopted, so the potential energy can be expressed as

$$\begin{aligned} \Pi(\boldsymbol{u}) = & \int_\Omega \frac{1}{2} \boldsymbol{\varepsilon}^{\mathrm{T}} \boldsymbol{\sigma} \mathrm{d}\Omega - \int_\Omega \boldsymbol{u}^{\mathrm{T}} \boldsymbol{b} \mathrm{d}\Omega - \int_{\Gamma_s} \boldsymbol{u}^{\mathrm{T}} \bar{\boldsymbol{p}} \mathrm{d}S \\ & + \int_{\Gamma_d} \frac{1}{2} \boldsymbol{k} (\boldsymbol{u} - \bar{\boldsymbol{u}})^{\mathrm{T}} (\boldsymbol{u} - \bar{\boldsymbol{u}}) \mathrm{d}S \end{aligned} \tag{26}$$

where Γ_s is the stress boundary, Γ_d is the displacement boundary, $\bar{\boldsymbol{u}}$ is the given displacement on Γ_d, $\bar{\boldsymbol{p}}$ is the given traction on Γ_s, $\boldsymbol{k}$ is the user-specified penalty.

The displacement approximations expressed by Eq. (20) or (25) can be rewritten as

$$\boldsymbol{u} = \boldsymbol{N}\boldsymbol{h} \tag{27}$$

where $\boldsymbol{N}$ is the shape function matrix, $\boldsymbol{h}$ is the degrees of freedom.

The strain $\boldsymbol{\varepsilon}$ and displacement $\boldsymbol{u}$ has the following relationship

$$\boldsymbol{\varepsilon} = \boldsymbol{L}_d \boldsymbol{u} \tag{28}$$

with

$$\boldsymbol{L}_d = \begin{bmatrix} \frac{\partial}{\partial x} & 0 & \frac{\partial}{\partial y} \\ 0 & \frac{\partial}{\partial y} & \frac{\partial}{\partial x} \end{bmatrix}^{\mathrm{T}} \tag{29}$$

Substituting Eq. (27) into Eq. (28), yields

$$\boldsymbol{\varepsilon} = \boldsymbol{B}\boldsymbol{h} \tag{30}$$

with

$$\boldsymbol{B} = \boldsymbol{L}_d \boldsymbol{N} \tag{31}$$

The stress $\boldsymbol{\sigma}$ and strain $\boldsymbol{\varepsilon}$ has the relationship as follows

$$\boldsymbol{\sigma} = \boldsymbol{D}\boldsymbol{\varepsilon} \tag{32}$$

where $\boldsymbol{D}$ is the elastic matrix.

Substituting Eq. (30) into Eq. (32), we have

$$\boldsymbol{\sigma} = \boldsymbol{S}\boldsymbol{h} \tag{33}$$

with

$$\boldsymbol{S} = \boldsymbol{D}\boldsymbol{B} \tag{34}$$

Substituting Eqs. (27), (30) and (33) into Eq. (26), yields the system of linear equilibrium equations

$$\boldsymbol{K}\boldsymbol{p} = \boldsymbol{q} \tag{35}$$

where $\boldsymbol{K}$ is the global stiffness matrix, $\boldsymbol{p}$ is the degrees of freedom including normal and enriched items on all the physical patches, $\boldsymbol{q}$ is the generalized force vector. Both $\boldsymbol{K}$ and $\boldsymbol{q}$ are obtained by assembling all the element stiffness matrices $\boldsymbol{K}^e$ and element load vector q^e, defined as

$$\boldsymbol{K}^e = \int_{\Omega^e} \boldsymbol{B}^T \boldsymbol{D} \boldsymbol{B} \mathrm{d}\Omega + \boldsymbol{k} \int_{\Gamma_d^e} \boldsymbol{N}^{\mathrm{T}} \boldsymbol{N} \mathrm{d}S \tag{36}$$

$$\boldsymbol{q}^e = \int_{\Omega^e} \boldsymbol{N}^T \boldsymbol{b} \mathrm{d}\Omega + \int_{\Gamma_s^e} \boldsymbol{N}^T \bar{\boldsymbol{p}} d\boldsymbol{S} + \boldsymbol{k} \int_{\Gamma_d^e} \boldsymbol{N}^T \bar{\boldsymbol{u}} d\boldsymbol{S} \tag{37}$$

respectively.

Since the manifold element in Quad4-CNS (NMM) can be in arbitrary shape, the manifold element should be firstly divided into a number of triangles (Fig. 2) and then Gauss quadrature rule is performed over each triangle. For the normal element, the Gauss quadrature rule over its triangular quadrature domains is performed. For blending element or singular element, the Gauss quadrature rule over its degenerated quadrilateral quadrature

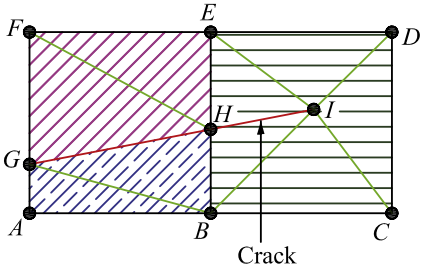

Fig. 2. Manifold elements divided into triangles to conduct Gaussian quadrature: blending manifold element *ABHG* is divided into two triangles, namely, △*ABG* and △*BHG*; blending manifold element *GHEF* is also divided into two triangles, namely, △*HEF* and △*HFG*; singular manifold element *BCDEH* is divided into five triangles, namely, △*BCI*, △*CDI*, △*DEI*,△*EHI* and △*HBI*.

domains is performed. Here, the degenerated quadrilateral quadrature domain is constructed by counting the third vertex of the triangle twice.

3.7. Numerical implementation procedure

The key steps of the numerical implementation procedure for the proposed Quad4-CNS (NMM) element are listed as follows:

(1) Divide the problem domain into a set of manifold elements and obtain the information on mathematical patches, physical patches, element connectivity, coordinates of nodes. Define material properties, loading and displacement boundary condition.
(2) Define the support order for boundary nodes: *first* or *second order support*.
(3) Define the initial crack information as a line by specifying the starting and ending points. Here, ending points are defined as crack-tip nodes.
(4) Loop over the number of incremental steps.
  (a) Select/update singular nodes (or singular physical patch) and store them into a set; Select/update support nodes for boundary nodes and internal nodes.
  (b) Loop over the manifold elements
    i. In each manifold element, the element support nodes are the union of the 4 sets of support nodes of its element connectivity.
    ii. Loop over the quadrature points
      1. Compute shape functions in Eq. (27).
      2. Compute the stiffness matrix as defined Eq. (36).
      3. Compute the force vector as defined in Eq. (37).
      4. Assemble the stiffness matrix and load vector into the global stiffness matrix and force vector.
    iii. End the loop over the quadrature points.
  (c) End the loop over the manifold elements.
  (d) Solve the linear system of algebraic equations to obtain $\boldsymbol{p}$ as defined Eq. (35).
  (e) Recovery of the stress and strain fields.
  (f) Calculate the SIFs using the interaction integral method.
  (g) Compute the crack propagation angle based on the information of the computed SIFs to determine the crack growth direction.
  (h) Specify a given size of crack growth, update the new crack line including the crack path and tips. Update the information on manifold elements, physical patches, element connectivity and coordinates of nodes.
(5) End the loop over the incremental steps.
(6) Visualization of the results.

4. SIFs implementation and crack growth simulation

Stress intensity factor (SIF) which could characterize the singularity strength of the displacement and stress distribution around the crack tip, is of great importance in the failure analysis. To obtain the SIFs, the domain form of interaction integrals [65,50] is employed in this paper. Two states of a cracked body are considered. State $1\left(\sigma_{ij}^{\text{real}},\ \varepsilon_{ij}^{\text{real}},\ u_i^{\text{real}}\right)$ corresponds to the actual state while state $2\left(\sigma_{ij}^{\text{aux}},\ \varepsilon_{ij}^{\text{aux}},\ u_i^{\text{aux}}\right)$ is an auxiliary state which is chosen as the asymptotic fields for modes I and II. The formulation for interaction integral with the mixed-mode SIFs can be written as [65,50]

$$I^{(\text{real,aux})} = -\int_{A_J}\left[W^{(\text{real,aux})}\delta_{1j} - \sigma_{ij}^{\text{real}}\frac{\partial u_i^{\text{aux}}}{\partial x_1} - \sigma_{ij}^{\text{aux}}\frac{\partial u_i^{\text{real}}}{\partial x_1}\right]\frac{\partial q}{\partial x_j}\,\mathrm{d}A \tag{38}$$

in which $W^{(\text{real,aux})}$ is the interaction strain energy defined as

$$W^{(\text{real,aux})} = \sigma_{ij}^{\text{real}}\varepsilon_{ij}^{\text{aux}} = \sigma_{ij}^{\text{aux}}\varepsilon_{ij}^{\text{real}}, \tag{39}$$

A_J is the area-path determined by a circle with radius R shown in Fig. 3. R is called domain radius and defined as

$$R = R_d h \tag{40}$$

in which h is the size of mathematical patch, namely, the maximum circumradius of a mathematical patch, R_d is a factor which can determine the size of the circle. $q(\boldsymbol{x})$ is a bounded weighting function, which is schematically represented in Fig. 3, the value of which is 1 within the circle and 0 outside the circle. Once $I^{(\text{real,aux})}$ is obtained, the value of SIFs including K_{I} and K_{II} could be calculated easily, see details in [65].

In theory, the value of interaction integral should be path independent. As a matter of fact, the value of interaction integral is path dependent due to the error in numerical integration. Therefore, the value of R will directly influence accuracy of the calculated SIFs by numerical methods, and an optimal R is of great importance in crack analysis. The optimal value of R for the developed Quad4-CNS (NMM) element will be discussed in Section 5.3.

After obtaining stress intensity factors, K_{I} and K_{II}, the maximum hoop-stress criterion [66,67] is adopted to evaluate the crack growth direction in this paper. This criterion states that the crack will grow from its tip in a radial direction at a critical angle, θ_c, so that the maximum circumferential stress reaches a critical material strength [66]. θ_c is calculated based on K_{I} and K_{II} as follows [67]

$$\theta_c = 2\tan^{-1}\left(\frac{1-\sqrt{1+8(K_{\text{II}}/K_{\text{I}})^2}}{4(K_{\text{II}}/K_{\text{I}})}\right) \tag{41}$$

5. Numerical examples

A set of numerical examples are carried out to assess the efficiency and accuracy of the present Quad4-CNS (NMM) model.

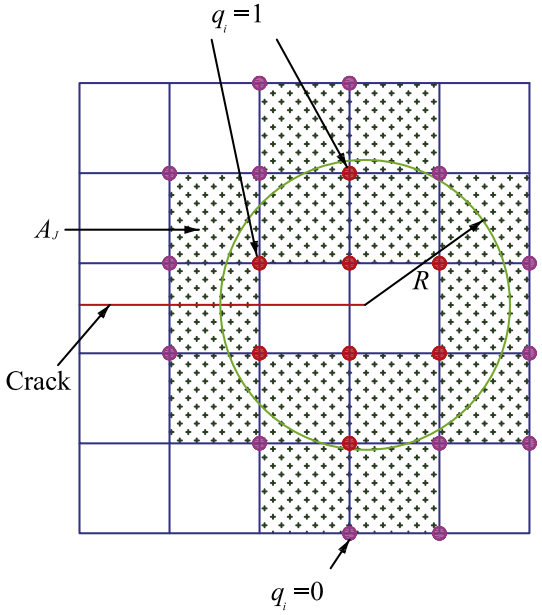

Fig. 3. Determination of area-path A_J for the interaction integral and weight function q.

Since Quad4-CNS (NMM) element can always adopt regular mesh without considering the problem domain boundary to construct the global approximation, regular mathematical mesh for Quad4-CNS (NMM) element will always be used in the rest of this paper to conduct these tests.

The number of polynomial terms to construct the local approximations of the Quad4-CNS (NMM) element will be taken according to the scheme presented in Section 3.2. As discussed in Section 3.2, in the present Quad4-CNS (NMM) element, the physical patch on the computational boundary will adopt *first order support* or *second order support* to obtain the support nodes, while for the physical patch within the computational domain, only the *first order support* is used. For the convenience of description, Quad4-CNS1 (NMM) means *first order support* is adopted for the physical patch on the computational boundary, while Quad4-CNS2 (NMM) means *second order support* is adopted for the physical patch on the computational boundary.

The physical units used in the present work are based on the international standard unit system. Here, n defines the total number of the nodes in the computational model. To assess accuracy and convergence, the relative L^2 errors in the displacement norm and in the energy norm are defined, respectively, as follows:

$$e_{\mathrm{d}} = \sqrt{\frac{\int_{\Omega}(\boldsymbol{u}^{\mathrm{ex}} - \boldsymbol{u}^{\mathrm{num}})^2 d\Omega}{\int_{\Omega}(\boldsymbol{u}^{\mathrm{ex}})^2 d\Omega}}, \tag{42}$$

$$e_{\mathrm{e}} = \sqrt{\frac{\frac{1}{2}\int_{\Omega}(\varepsilon^{\mathrm{ex}} - \varepsilon^{\mathrm{num}})^{\mathrm{T}}\boldsymbol{D}(\varepsilon^{\mathrm{ex}} - \varepsilon^{\mathrm{num}})d\Omega}{\frac{1}{2}\int_{\Omega}(\varepsilon^{\mathrm{ex}})^{\mathrm{T}}\boldsymbol{D}(\varepsilon^{\mathrm{ex}})d\Omega}}, \tag{43}$$

where the superscript "ex" represents the exact or analytical solution and the superscript "num" denotes a numerical solution.

5.1. Linear dependence test

A known problem of PU-based methods with high order global approximation is the linear dependence problem, which leads to the rank deficiency of global (stiffness) matrices [57]. The material parameters in this test are listed as Young's modulus $E = 1.0$, Poisson's ratio $v = 0.25$, and the plane stress condition is assumed. The meshes for this test are shown in Fig. 4. The number of computed zero eigenvalues for both Quad4-CNS1 (NMM) and Quad4-CNS2 (NMM) elements is shown in Table 1. According to the numerical tests, before applying boundary condition, a total of three zero eigenvalues (corresponding to the three rigid body modes) are found for all the meshes in both Quad4-CNS1 (NMM) and Quad4-CNS2 (NMM) elements. The number of zero eigenvalues is also found to be invariant with respect to the mesh geometry and mesh refinement. Moreover, by applying the boundary conditions, there are no more zero eigenvalues left. This suggests that the proposed Quad4-CNS (NMM) element is free of linear dependence problem.

5.2. Cantilever beam subject to a tip-shear force

A two dimensional cantilever beam subjected to a tip-shear force with length L, height D, and the unit thickness is studied for the various behaviors of Quad4-CNS (NMM) element as a benchmark problem. The beam is fixed at the left end and subjected to a parabolic traction P at the free end in Fig. 5. The analytical solution is available and can be found in reference [68]:

$$u_x = \frac{Py}{6EI}\left[(6L - 3x)x + (2 + v)\left(y^2 - \frac{D^2}{4}\right)\right], \tag{44}$$

$$u_y = -\frac{P}{6EI}\left[3vy^2(L - x) + (4 + 5v)\frac{D^2 x}{4} + (3L - x)x^2\right], \tag{45}$$

where, the moment of inertia I for a beam with rectangular cross section and unit thickness is given by $I = D^3/12$.

The stress corresponding to the displacements are

$$\sigma_{xx}(x,y) = \frac{P(L-x)y}{I}, \quad \sigma_{yy}(x,y) = 0, \quad \tau_{xy}(x,y) = -\frac{P}{2I}\left(\frac{D^2}{4} - y^2\right). \tag{46}$$

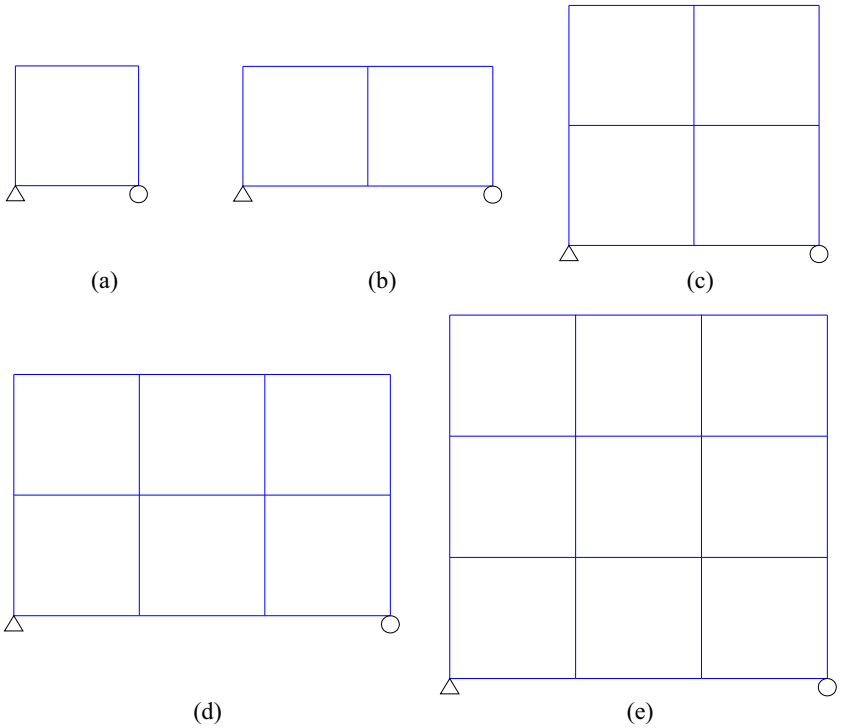

Fig. 4. Meshes for investigation of linear dependence issue (△-constrains in both the x- and y-directions, ○-constrains in the y-direction).

Table 1
Nullity of stiffness matrices of Quad4-CNS1(NMM) and Quad4-CNS2(NMM) elements, see Fig. 4 for the meshes.

Mesh	Total DOfs	Quad4-CNS1(NMM)		Quad4-CNS2(NMM)	
		Nullity DOfs (without essential boundary treatment)	Nullity DOfs (apply essential boundary treatment)	Nullity DOfs (without essential boundary treatment)	Nullity DOfs (apply essential boundary treatment)
(a)	8	3	0	3	0
(b)	12	3	0	3	0
(c)	18	3	0	3	0
(d)	24	3	0	3	0
(e)	32	3	0	3	0

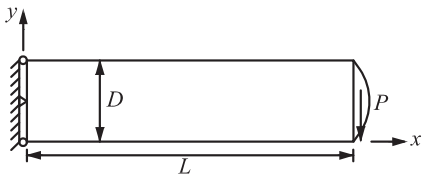

Fig. 5. A cantilever beam subjected to a tip-shear force on the right end.

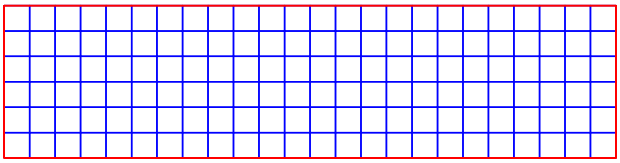

(a) mesh A (175 nodes)

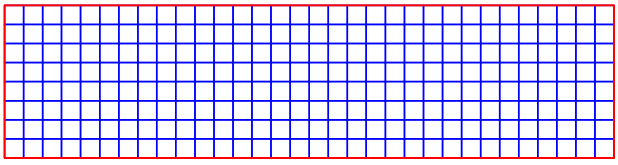

(b) mesh B (297 nodes)

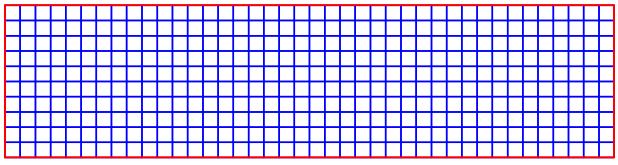

(c) mesh C (451 nodes)

Fig. 6. Mesh for cantilever beam subjected to a tip-shear force.

The parameters in the computation are taken as $L = 48$, $D = 12$, $P = 1000$, $E = 3.0 \times 10^7$, $v = 0.3$, and the plane stress condition is assumed. In the computation, the points on the boundary of $x = 0$ are constrained using the exact displacements given from the analytical solutions, and the traction is specified on the boundary at $x = L$ using the analytical solutions.

To examine the convergence of numerical solutions in Quad4-CNS (NMM) element, three discrete models with regular grids are constructed as shown in Fig. 6. The convergence curves are plotted in Fig. 7. Accuracy of Quad4-CNS1 (NMM) and Quad4-CNS2 (NMM) elements in both displacement norm and energy norm are compared to Trig3 (NMM) and Quad4 (NMM) elements.

The numerical results of Quad4-CNS1 (NMM) element are all significantly better than those of Trig3 (NMM) and Quad4 (NMM) element in both the displacement and energy norm. Through increasing the support order (second order support is adopted) of physical patches on the computational boundary, the performance of Quad4-CNS2 (NMM) element is even much better than that of Quad4-CNS1 (NMM) element. However, the extra computational cost for Quad4-CNS2 (NMM) element is limited as compared to Quad4-CNS1 (NMM) element.

The convergence rates of Quad4-CNS1 (NMM) and Quad4-CNS2 (NMM) elements are −3.89 and −2.79 respectively in the displacement norm, which are all significantly better than the convergence rates of Trig3 (NMM) (−2.03) and Quad4 (−2.14). The convergence rate of Quad4-CNS1 (NMM) element is −1.62 in the energy norm, which is also significantly better than the convergence rates of Trig3 (NMM) (−1.02) and Quad4 (NMM) (−1.07). The convergence rate of Quad4-CNS2 (NMM) element, however, is comparable to that of Trig3 (NMM) and Quad4 (NMM) elements in the energy norm.

Fig. 8 shows the contour of σ_x on the regular mesh for Trig3 (NMM), Quad4 (NMM) and Quad4-CNS2 (NMM) elements. It can be found that the global stress field of Quad4-CNS2 (NMM) ele-

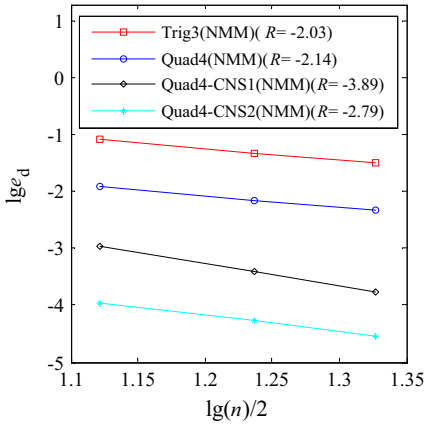

(a) Relative error in displacement norm

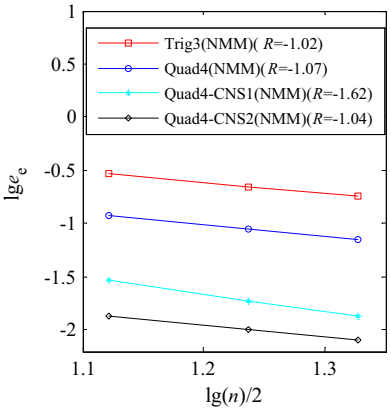

(b) Relative error in energy norm

Fig. 7. Comparison of accuracy for cantilever beam problem subjected to a tip-shear force (see Fig. 6 for the mesh).

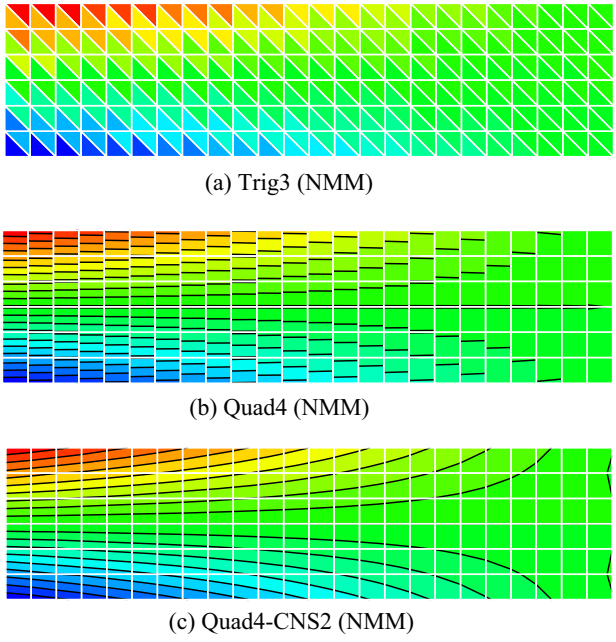

(a) Trig3 (NMM)

(b) Quad4 (NMM)

(c) Quad4-CNS2 (NMM)

Fig. 8. Contour plot of σ_x for the cantilever beam subjected to a tip-shear force (see Fig. 6(a) for the mesh).

ment is smoother than that of Trig3 (NMM) and Quad4 (NMM) elements.

5.3. An edge crack under tensile load

In this section, the simplest fracture problem, a finite rectangular plate with an edge crack subjected to a uniform tensile load on the top of the plate, as shown in Fig. 9, is considered. The geometry and the boundary conditions are schematically depicted in Fig. 9 (a). Fig. 9(b) displays an example mathematical mesh with 19×39 layers for this problem. The parameters in the computation are taken as $H = 8$, $W = 7$, $\sigma = 1$, $E = 3.0 \times 10^7$, $\nu = 0.25$, $a = 3.5$, and the plane strain condition is assumed. The analytical solution of SIFs for such a structure is given by Ewalds and Wanhill [69]:

$$K_I = C\sigma\sqrt{\pi a}, \tag{47}$$

where the correction coefficient is determined by

$$C = 1.12 - 0.231\left(\frac{a}{W}\right) + 10.55\left(\frac{a}{W}\right)^2 - 21.72\left(\frac{a}{W}\right)^3 + 30.39\left(\frac{a}{W}\right)^4. \tag{48}$$

The influence of R, as depicted in Fig. 3, on the SIFs in terms of the developed Quad4-CNS2 (NMM) element is numerically investigated. Three different values of R_d (defined in Eq. (40)) such as $R_d = 2$, 2.5, and 3 are taken while three regular mathematical meshes with 19×39, 29×59 and 39×79 layers are used. Convergence of the normalized SIFs against mesh density for this problem is given in Table 2. Accuracy of Quad4-CNS2 (NMM) element is com-

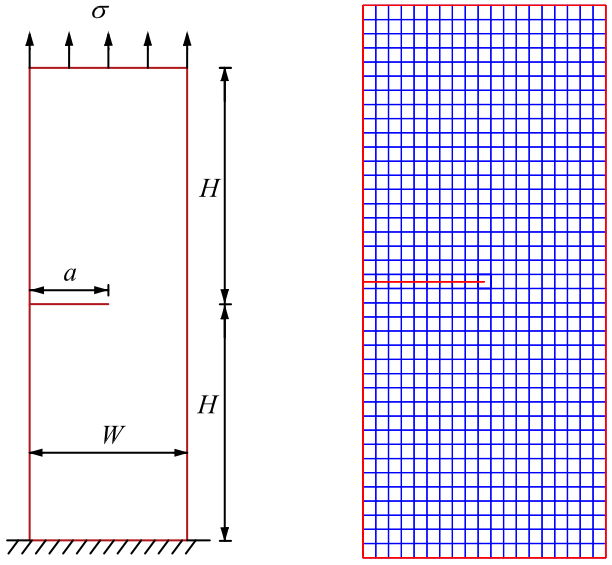

(a) The geometry and the boundary conditions

(b) example mesh with 19×39 layers

Fig. 9. An edge-cracked plate subjected to a uniform tensile loading.

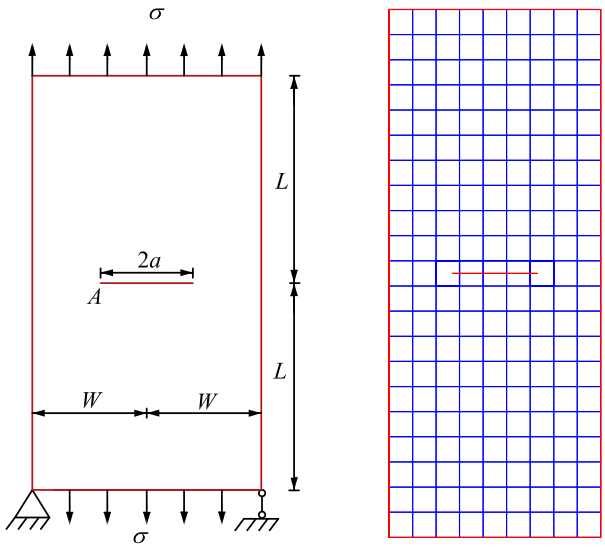

(a) The geometry and the boundary conditions

(b) example mesh with 9 × 21 layers

Fig. 10. A rectangular plate with a central crack subjected to tension.

Table 2
Convergence of normalized SIFs against mesh density for an edge crack under tensile loading.

Element type	Normalized SIFs	R	Mesh		
			19×39	29×59	39×79
Quad4-CNS2(NMM)	M_I	2.0	0.975	0.988	0.994
		2.5	0.966	0.978	0.984
		3.0	0.968	0.980	0.986
XQ4 [50]	M_I	2.0	0.972	0.983	0.989
		2.5	0.967	0.978	0.984
XCQ4 [50]	M_I	2.0	0.976	0.988	0.993
		2.5	0.971	0.983	0.988

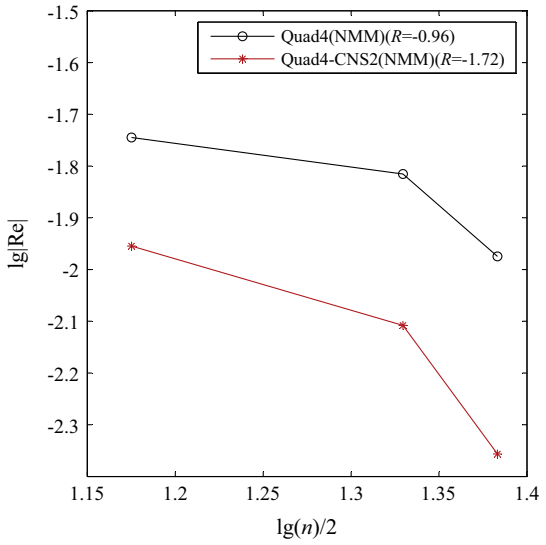

Fig. 11. Convergence rates in relative errors of SIFs at crack tip *A* for the rectangular plate with a central crack subjected to tension.

pared with extended quadrilateral element (XQ4) and extended consecutive-interpolation quadrilateral element (XCQ4) [50].

It is obvious that the accuracy of the SIFs increases and approaches to the exact solutions with increasing the number of element layers. The variation of selected R shows some effects on the accuracy of SIFs. The optimum R_d for Quad4-CNS2 (NMM) element in this test is 2.0. When R_d is set to be 2.0, accuracy of the developed Quad4-CNS2 (NMM) element is slightly better than that of XQ4 and XCQ4 elements.

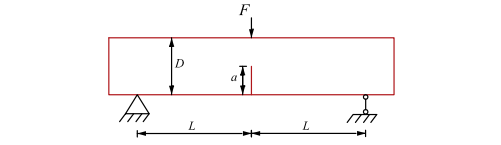

(a) The geometry and the boundary conditions

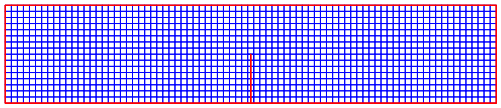

(b) a mesh with 81×16 layers

Fig. 12. A three-point bending test specimen.

5.4. A plate with a central crack subjected to tensile forces

As the second example for crack analysis, a rectangular plate of homogeneous isotropic material with a horizontal central crack under the action of uniform tension in the vertical direction is considered. The geometry and the boundary conditions are schematically depicted in Fig. 10(a). Fig. 10(b) displays an example mathematical mesh with 9×21 layers for this problem. Under this setting, the fracture is of pure mode I. The parameters are $W = 10.0$ cm, $L = 25.0$ cm, $a = 4$ cm, and $\sigma = 1$ N/cm^2, Young's modules $E = 3 \times 10^7$ N/cm^2 and Poisson's ratio $\upsilon = 0.25$. The plane strain condition is assumed. The analytical solution of SIFs for such a structure is given by [70],

$$K_I = C\sigma\sqrt{a\pi} \tag{49}$$

where C is the modification factor to reflect the size effect, approximated by

$$C = \left[1 - 0.025\left(\frac{a}{W}\right)^2 - 0.06\left(\frac{a}{W}\right)^4\right]\left(\sec\left(\frac{\pi a}{2W}\right)\right)^{0.5} \tag{50}$$

Based on the formula present in Eq. (49), the analytical value for this plate is $K_I = 3.9315$ Ncm$^{-3/2}$ [71]. Convergence of the relative errors in SIFs (Re) against the number of nodes for this problem is given in Fig. 11. Accuracy of Quad4-CNS2 (NMM) element is compared with Quad4 (NMM) element.

The numerical results of Quad4-CNS2 (NMM) element are significantly better than those of Quad4 (NMM) element for this problem. The convergence rate of Quad4-CNS2 (NMM) elements is -1.72 which is significantly better than that of Quad4 (NMM) element (-0.96).

5.5. Crack growth in a three-point bend specimen

In the previous two examples, the Quad4-CNS2 (NMM) element has shown its ability to accurately calculate the SIFs. Since the SIFs are very important factors in the prediction of crack propagation direction, the present Quad4-CNS2 (NMM) element should be a versatile and promising approach in solving crack propagation problems.

As the first example for crack propagation, a three-point bending specimen under a concentrated load $F = 1$ and shown in Fig. 12, is considered. The geometry and the boundary conditions are schematically depicted in Fig. 12(a). Fig. 12(b) displays the mesh for this problem. The parameters in the computation are taken as $D = 6$, $L = 12$, $\tau = 1$, $E = 2.0 \times 10^8$, $\upsilon = 0.25$, $a = 3$, and the plane strain condition is assumed.

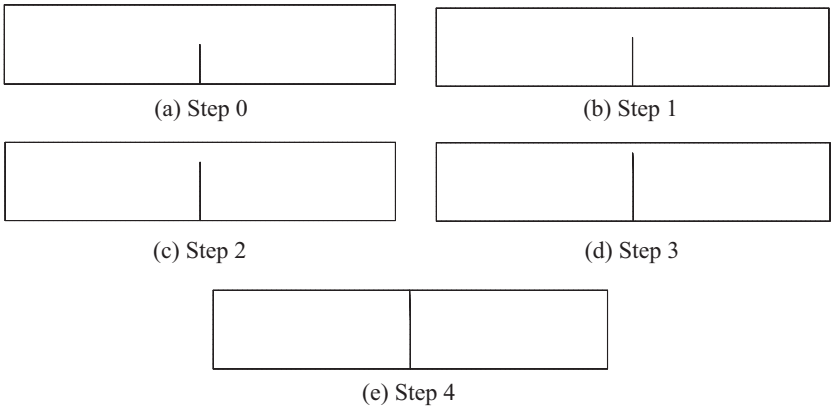

(a) Step 0 (b) Step 1

(c) Step 2 (d) Step 3

(e) Step 4

Fig. 13. Propagation of the crack path for a three-point bending test specimen.

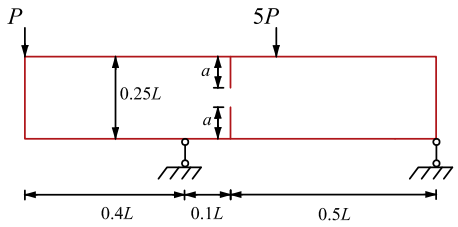

(a) The geometry and the boundary conditions

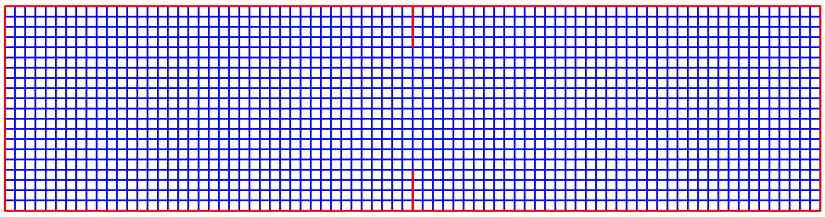

(b) a mesh with 80×20 layers

Fig. 14. A beam under four-point loading.

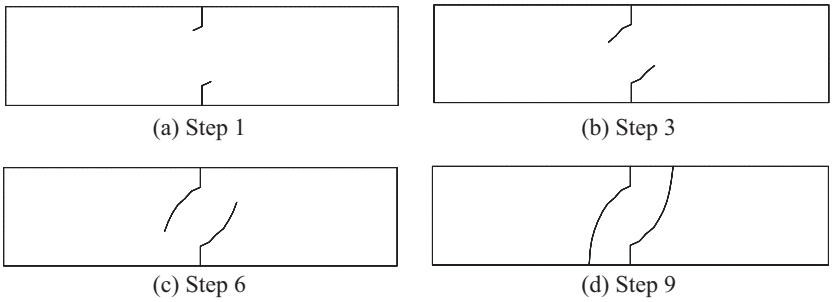

(a) Step 1 (b) Step 3

(c) Step 6 (d) Step 9

Fig. 15. Propagation of the crack path in a beam under four-point loading by the Quad4-CNS2 (NMM) element.

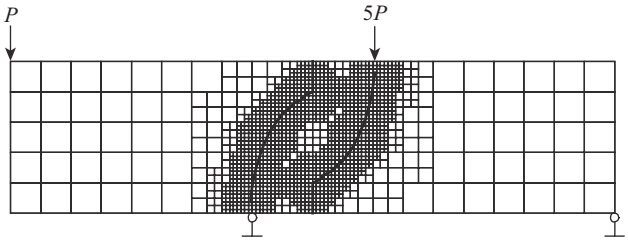

Fig. 16. Propagation of the crack path in a beam under four-point loading by the virtual node method for polygonal element [72].

Since this example is a pure mode I problem, the crack propagation path should be a vertical line. The propagation of crack path by the present Quad4-CNS2 (NMM) element is shown in Fig. 13. It is obviously that the Quad4-CNS2 (NMM) element accurately predicts the propagation of crack path and agrees well with the theoretical prediction.

5.6. Crack growth in a beam under four-point loading

As the second example for crack propagation, a pre-cracked beam subjected to four-point shear loading is considered. This example has been studied by Tang et al. [72] using the virtual node method for polygonal element (VNMPE). The geometry and the boundary conditions are schematically depicted in Fig. 14(a). Fig. 14(b) displays the mesh for this problem. The parameters in the computation are taken as $L = 4$, $P = 1$, $E = 2.0 \times 10^8$, $v = 0.25$,

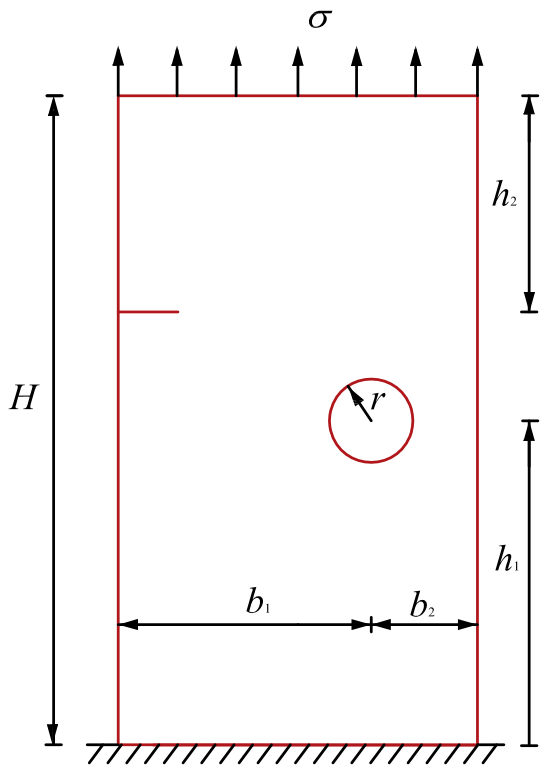

Fig. 17. A perforated plate with a circle hole subjected to a uniform tensile loading.

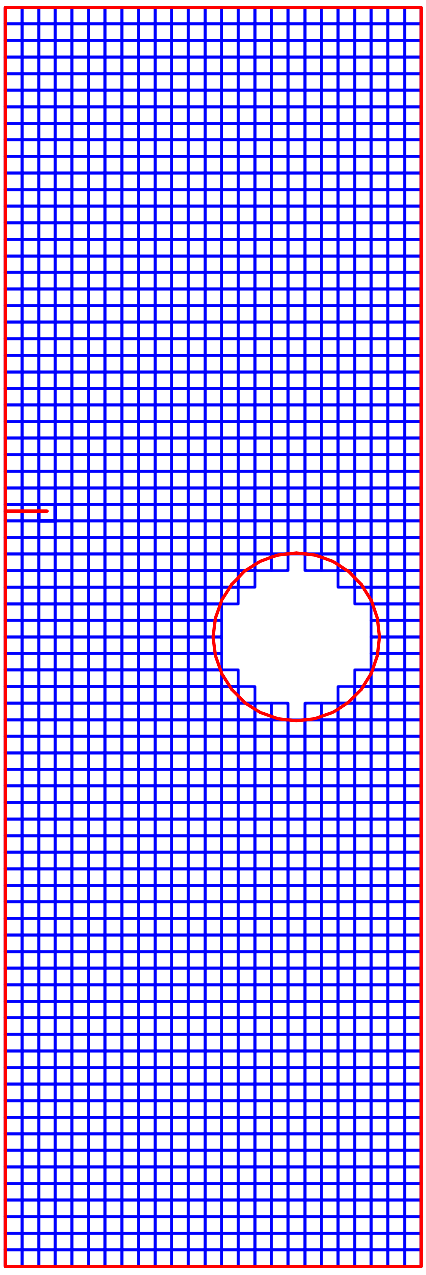

Fig. 18. Mesh for plate with a circle hole subjected to a uniform tensile loading (Mesh with 25 × 76 layers, 1962PPs).

$a = 0.2$, and the plane strain condition is assumed. The crack path of crack propagation obtained by the Quad4-CNS2 (NMM) element is shown in Fig. 15. As expected, the propagation of the crack path is well consistent with that predicted by the VNMPE [72], see Fig. 16. Initially, the cracks move away from each other, and finally they all move toward the loading points.

5.7. Crack growth in a perforated panel with a circular hole

As the final example for crack propagation, a perforated plate with a fixed bottom edge and subjected to a uniform tensile load σ at the top edge as schematically depicted in Fig. 17 is considered. This example has been studied by Leonel and Venturini [73] using BEM, and by Nguyen et al. [66] using extended mesh free Galerkin radial point interpolation method (X-RPIM). Fig. 18 displays the mesh for this problem. The parameters in the computation are taken as $H = 3$; $h_1 = 1.5$; $h_2 = 1.2$; $b_1 = 0.7$; $b_2 = 0.3$; initial crack

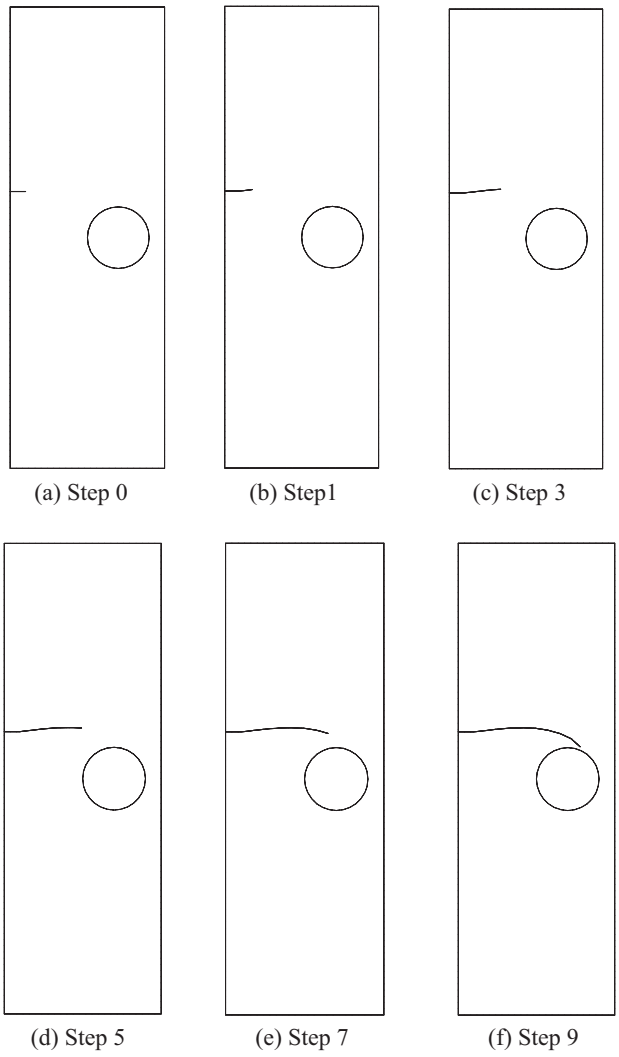

Fig. 19. Propagation of the crack path in a perforated panel subjected to a uniform tensile loading by the Quad4-CNS2 (NMM) element.

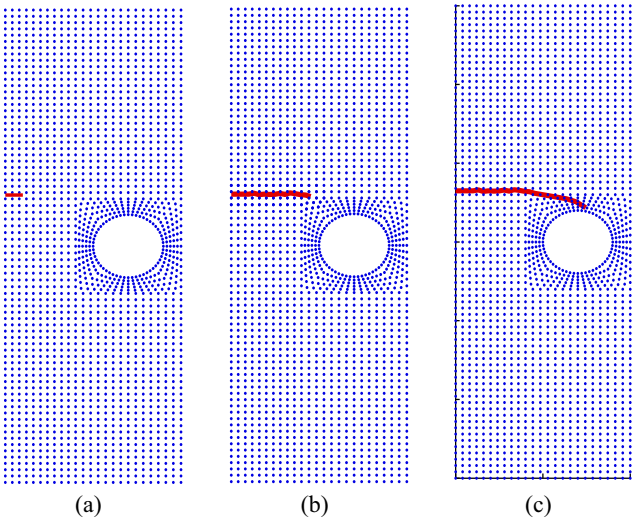

Fig. 20. Propagation of the crack path in a perforated panel subjected to a uniform tensile loading by the extended meshfree Galerkin radial point interpolation method [66].

length $a = 0.1$; $\sigma = 5000$, $E = 3.0 \times 10^7$, $v = 0.2$, and the plane strain condition is assumed. The crack growth paths obtained by the Quad4-CNS2 (NMM) element are shown in Fig. 19. As expected, the propagation of the crack path is well consistent with that predicted by both the BEM and X-RPIM, see Fig. 20. As already stated in [73,66] and again found in this study that the crack tip approaches the hole, it turns toward the hole and finally collapses with the hole.

6. Discussions and conclusions

In this study, a four-node quadrilateral element fitted to the numerical manifold method with continuous nodal stress named as Quad4-CNS (NMM) element has been built. This element performs excellently for linear elastic continuous and fracture problems. Some important observations from this work are as follows:

(1) The stress field of Quad4-CNS (NMM) element is continuous at the nodes. With this advantage, the nodal stress can be conveniently obtained without any smoothing operation.
(2) The present Quad4-CNS (NMM) element is free from the "linear dependence" issue which otherwise cripples many of the partition of unity based methods with high order approximation.
(3) Inheriting all the advantage from numerical manifold method (NMM), Quad4-CNS (NMM) element is very suitable to solve crack propagation problems, because Quad4-CNS (NMM) element can always adopt regular mesh without considering the problem domain boundary to construct the global approximation.
(4) In solving the linear elastic continuous problem, accuracy of Quad4-CNS1 (NMM) (*first order support* is adopted for the physical patches on the computational boundary) element is generally better than that given by Trig3 (NMM) and Quad4 (NMM) elements. The results obtained from the Quad4-CNS1 (NMM) element also exhibit a faster convergence than Trig3 (NMM) and Quad4 (NMM) elements. The present Quad4-CNS2 (NMM) (*second order support* is adopted for the physical patches on the computational boundary) element gives much better results compared to Trig3 (NMM), Quad4 (NMM) and Quad4-CNS1 (NMM) elements.
(5) In solving the fracture problems, if proper interaction integral radius is adopted, the present Quad4-CNS2 (NMM) element generally obtains higher accuracy than both extended quadrilateral element (XQ4) and extended consecutive-interpolation quadrilateral element (XCQ4) [50].
(6) In the crack propagation analysis, the propagation of the crack paths obtained by Quad4-CNS2 (NMM) element are consistent with those predicted by other numerical and theoretical methods.

Without increasing the number of nodes, Quad4-CNS (NMM) provides alternative approach to improve accuracy of traditional NMM, however this increases the bandwidth of the global stiffness matrix and increases the computational time. Considering the whole computation process comprehensively, as Quad4-CNS (NMM) is able to obtain much better results than traditional NMM under the same mesh, it decrease the time to generate very fine discretized model, which is normally time consuming. In addition, Quad4-CNS (NMM) does not require extra time to smooth nodal stress.

In view of the advantages of the Quad4-CNS (NMM) element, it is worth to further study and apply it to other fields such as seepage, heat conduction and elastic-plastic problems. It is also worth to extend the two dimensional Quad4-CNS (NMM) element to its three-dimensional version to solve more realistic problems. It is noticed the present work is still very preliminary. In the following work, we will apply the present Quad4-CNS (NMM) element to static and dynamic multiple crack propagation problems.

Acknowledgements

This study is supported by the National Natural Science Foundation of China, under the Grant Nos. 51609240, 11572009, 51538001, U1402231 and 51509241, and the National Basic Research Program of China (973 Program), under the Grant No. 2014CB047100.

References

[1] Zienkiewicz OC, Taylor RL. The finite element method. 5th ed. Oxford: Butterworth-Heinemann; 2000.
[2] Paluszny A, Tang XH, Zimmerman RW. Fracture and impulse based finite-discrete element modelling of fragmentation. Comput Mech 2013;52(5):1071–84.
[3] Tang XH, Paluszny A, Zimmerman RW. Energy conservative property of impulse-based methods for collision resolution. Int J Numer Meth Eng 2013;95(6):529–40.
[4] Karihaloo BL, Xiao QZ. Modeling of stationary and growing cracks in FE framework without remeshing: a state-of-the-art review. Comput Struct 2003;81:119–29.
[5] Areias P, Rabczuk T, Dias-da-Costa D. Element-wise fracture algorithm based on rotation of edges. Eng Fract Mech 2013;110:113–37.
[6] Areias P, Rabczuk T. Finite strain fracture of plates and shells with configurational forces and edge rotation. Int J Numer Meth Eng 2013;94(12):1099–122.
[7] Areias P, Rabczuk T, Camanho PP. Finite strain fracture of 2D problems with injected anisotropic softening elements. Theoret Appl Fract Mech 2014;72:50–63.
[8] Rabczuk T, Belytschko T. Cracking particles: a simplified mesh-free method for arbitrary evolving cracks. Int J Numer Meth Eng 2004;61(13):2316–43.
[9] Bordas S, Rabczuk T, Zi G. Three-dimensional crack initiation, propagation, branching and junction in non-linear materials by an extended meshfree method without asymptotic enrichment. Eng Fract Mech 2008;75(5):943–60.
[10] Belytschko T, Lu YY, Gu L. Element-free Galerkin method. Int J Numer Meth Eng 1994;37(2):229–56.
[11] Zhuang XY, Augarde C. Aspects of the use of orthogonal basis functions in the element free Galerkin method. Int J Numer Meth Eng 2010;81:366–80.
[12] Zhuang X, Augarde C, Mathisen K. Fracture modelling using meshless methods and level sets in 3D: framework and modelling. Int J Numer Meth Eng 2012;92:969–98.
[13] Liu WK, Jun S, Zhang YF. Reproducing kernel particle methods. Int J Numer Meth Eng 1995;20(8–9):1081–106.
[14] Rabczuk T, Belytschko T, Xiao SP. Stable particle methods based on Lagrangian kernels. Comput Meth Appl Mech Eng 2004;193(12–14):1035–63.
[15] Zhuang X, Cai Y, Augarde C. A meshless sub-region radial point interpolation method for accurate calculation of crack tip fields. Theoret Appl Fract Mech 2014;69:118–25.
[16] Tanaka S, Suzuki H, Sadamoto S, Sannomaru S, Yu T, Bui TQ. J-integral evaluation for 2D mixed-mode crack problems employing a meshfree stabilized conforming nodal integration method. Comput Mech 2016;58:185–98.
[17] Zheng C, Wu SC, Tang XH, Zhang JH. A novel twice-interpolation finite element method for solid mechanics problems. Acta Mech Sin 2010;26(2):265–78.
[18] Liu GR, Gu YT. Meshless local Petrov–Galerkin (MLPG) method in combination with finite element and boundary element approaches. Comput Mech 2000;26(6):536–46.
[19] Rabczuk T, Xiao SP, Sauer M. Coupling of mesh-free methods with finite elements: basic concepts and test results. Commun Numer Meth Eng 2006;22:1031–65.
[20] Belytschko T, Black T. Elastic crack growth in finite elements with minimal remeshing. Int J Numer Meth Eng 1999;45(5):601–20.
[21] Babuška I, Melenk JM. The partition of unity method. Int J Numer Meth Eng 1997;40:727–58.
[22] Talebi H, Samaniego C, Samaniego E, Rabczuk T. On the numerical stability and mass-lumping schemes for explicit enriched meshfree methods. Int J Numer Meth Eng 2012;89(8):1009–27.
[23] Ghorashi S, Valizadeh N, Mohammadi S, Rabczuk T. T-spline based XIGA for fracture analysis of orthotropic media. Comput Struct 2015;147:138–46.
[24] Sukumar N, Chopp DL, Moës N, Belytschko T. Modeling holes and inclusions by level sets in the extended finite-element method. Comput Meth Appl Mech Eng 2001;190(46):6183–200.
[25] Bui TQ, Hirose S, Zhang C, Rabczuk T, Wu CT, Saitoh T, et al. Extended isogeometric analysis for dynamic fracture in multiphase piezoelectric/piezomagnetic composites. Mech Mater 2016;97:135–63.

[26] Bui TQ. Extended isogeometric dynamic and static fracture analysis for cracks in piezoelectric materials using NURBS. Comput Meth Appl Mech Eng 2015;295:470–509.
[27] Yu T, Bui TQ, Liu P, Zhang C, Hirose S. Interfacial dynamic impermeable cracks analysis in dissimilar piezoelectric materials under coupled electromechanical loading with the extended finite element method. Int J Solids Struct 2015;67:205–18.
[28] Bui TQ, Zhang C. Analysis of generalized dynamic intensity factors of cracked magnetoelectroelastic solids by X-FEM. Finite Elem Anal Des 2013;69:19–36.
[29] Bui TQ, Zhang C. Extended finite element simulation of stationary dynamic cracks in piezoelectric solids under impact loading. Comput Mater Sci 2012;62:243–57.
[30] Yu T, Bui TQ, Yin S, Doan DH, Wu CT, Van Do T, et al. On the thermal buckling analysis of functionally graded plates with internal defects using extended isogeometric analysis. Compos Struct 2016;136:684–95.
[31] Bhardwaj G, Singh IV, Mishra BK, Bui TQ. Numerical simulation of functionally graded cracked plates using NURBS based XIGA under different loads and boundary conditions. Compos Struct 2015;126:347–59.
[32] Doan DH, Bui TQ, Duc ND, Fushinobu K. Hybrid phase field simulation of dynamic crack propagation in functionally graded glass-filled epoxy. Compos B Eng 2016;99:266–76.
[33] Liu P, Yu T, Bui TQ, Zhang C, Xu Y, Lim CW. Transient thermal shock fracture analysis of functionally graded piezoelectric materials by the extended finite element method. Int J Solids Struct 2014;51(11):2167–82.
[34] Bhattacharya S, Singh IV, Mishra BK, Bui TQ. Fatigue crack growth simulations of interfacial cracks in bi-layered FGMs using XFEM. Comput Mech 2013;52 (4):799–814.
[35] Zhang X, Bui TQ. A fictitious crack XFEM with two new solution algorithms for cohesive crack growth modeling in concrete structures. Eng Comput 2015;32 (2):473–97.
[36] Shi GH. Manifold method of material analysis. In: Proceedings of the transactions of the ninth army conference on applied mathematics and computing. p. 57–76.
[37] Cai Y, Zhu H, Zhuang X. A continuous/discontinuous deformation analysis (CDDA) method based on deformable blocks for fracture modelling. Front Struct Civil Eng 2014;7:369–78.
[38] Fu XD, Sheng Q, Zhang YH, Zhou YQ, Dai F. Boundary setting method for the seismic dynamic response analysis of engineering rock mass structures using the discontinuous deformation analysis method. Int J Numer Anal Meth Geomech 2015;39(15):1693–712.
[39] Fu XD, Sheng Q, Zhang YH, Chen J. Application of the discontinuous deformation analysis method to stress wave propagation through a one-dimensional rock mass. Int J Rock Mech Min Sci 2015;80:155–70.
[40] Chiou YJ, Lee YM, Tsay RJ. Mixed mode fracture propagation by manifold method. Int J Fract 2002;114:327–47.
[41] Zheng H, Liu F, Du XL. Complementarity problem arising from static growth of multiple cracks and MLS-based numerical manifold method. Comput Meth Appl Mech Eng 2015;295:150–71.
[42] Ma GW, An XM, Zhang HH, Li LX. Modelling complex crack problems using the numerical manifold method. Int J Fract 2009;156:21–35.
[43] Wu ZJ, Wong LNY, Fan LF. Dynamic study on fracture problems in viscoelastic sedimentary rocks using the numerical manifold method. Rock Mech Rock Eng 2013;46(6):1415–27.
[44] Zheng H, Liu ZJ, Ge XR. Numerical manifold space of Hermitian form and application to Kirchhoff's thin plate problems. Int J Numer Meth Eng 2013;95:721–39.
[45] Jiang QH, Deng SS, Zhou CB, Lu WB. Modeling unconfined seepage flow using three-dimensional numerical manifold method. J Hydrodyn 2010;22:554–61.
[46] Zheng H, Liu F, Li CG. Primal mixed solution to unconfined seepage flow in porous media with numerical manifold method. Appl Math Model 2015;39:794–808.
[47] Lee NS, Bathe KJ. Effects of element distortions on the performance of isoparametric elements. Int J Numer Meth Eng 1993;36(20):3553–76.
[48] Tang XH, Zheng C, Wu SC, Zhang JH. A novel four-node quadrilateral element with continuous nodal stress. Appl Math Mech 2009;30(12):1519–32 (English Edition).
[49] Bui QT, Vo QD, Zhang Ch, Nguyen DD. A consecutive-interpolation quadrilateral element (CQ4): formulation and applications. Finite Elem Anal Des 2014;84:14–31.
[50] Kang ZY, Bui QT, Nguyen DD, Saitoh T, Hirose S. An extended consecutive-interpolation quadrilateral element (XCQ4) applied to linear elastic fracture mechanics. Acta Mech 2015;226(12):3991–4015.
[51] Zhang BR, Rajendran S. 'FE-meshfree' QUAD4 element for free-vibration analysis. Comput Meth Appl Mech Eng 2008;197(45–48):3595–604.
[52] Wu SC, Zhang WH, Peng X, Miao BR. A twice-interpolation finite element method (TFEM) for crack propagation problems. Int J Comput Meth 2012;9:1250055.
[53] Zheng H, Xu DD. New strategies for some issues of numerical manifold method in simulation of crack propagation. Int J Numer Meth Eng 2014;97 (13):986–1010.
[54] Williams ML. On the stress distribution at the base of a stationary crack. J Appl Mech 1957;24:109–14.
[55] Strouboulis T, Babuška I, Copps K. The design and analysis of the generalized finite element method. Comput Meth Appl Mech Eng 2000;181(1–3):43–69.
[56] Cai YC, Zhuang XY, Augarde C. A new partition of unity finite element free from linear dependence problem and processing the delta property. Comput Meth Appl Mech Eng 2010;199:1036–43.
[57] Tian R, Yagawa G, Terasaka H. Linear dependence of unity-based generalized FEMs. Comput Meth Appl Mech Eng 2006;195(37–40):4768–82.
[58] Yang YT, Chen L, Xu DD, Zheng H. Free and forced vibration analyses using the four-node quadrilateral element with continuous nodal stress. Eng Anal Boundary Elem 2016;70:1–11.
[59] Xu JP, Rajendran S. A 'FE-Meshfree' TRIA3 element based on partition of unity for linear and geometry nonlinear analyses. Comput Mech 2013;51(6):843–64.
[60] Yang YT, Tang XH, Zheng H. Construct 'FE-Meshfree' Quad4 using mean value coordinates. Eng Anal Boundary Elem 2015;59:78–88.
[61] Yang YT, Tang XH, Zheng H. A three-node triangular element with continuous nodal stress. Comput Struct 2014;141:46–58.
[62] Liu G, Gu YT. A local radial point interpolation method (LRPIM) for free vibration analyses of 2-d solids. J Sound Vib 2001;246(1):29–46.
[63] Parlett BN. The symmetric eigenvalue problem. Prentice-Hall; 1980.
[64] Zheng C, Tang XH, Zhang JH, Wu SC. A novel mesh-free poly-cell Galerkin method. Acta Mech Sin 2009;25(4):517–27.
[65] Moes N, Dolbow J, Belytschko T. A finite element method for crack growth without remeshing. Int J Numer Meth Eng 1999;46:131–50.
[66] Nguyen NT, Bui TQ, Zhang CZ, Truong TT. Crack growth modeling in elastic solids by the extended meshfree Galerkin radial point interpolation method. Eng Anal Boundary Elem 2014;44:87–97.
[67] Erdogan F, Sih G. On the crack extension in plates under plane loading and transverse shear. J Basic Eng 1963;85:519–27.
[68] Timoshenko SP, Goodier JN. Theory of elasticity. 3rd ed. New York, U. K.: Mcgraw-Hill College; 1970.
[69] Ewalds H, Wanhill R. Fracture mechanics. New York: Edward Arnold; 1989.
[70] Tada H, Paris PC, Irwin GR. The stress analysis of cracks handbook. New York: ASME Press; 2000.
[71] Liu GR, Nguyen-Thoi T. Smoothed finite element methods. New York: CRC Press; 2010.
[72] Tang XH, Wu SC, Zheng C, Zhang JH. A novel virtual node method for polygonal elements. Appl Math Mech 2009;30(10):1233–46 (English Edition).
[73] Leonel DE, Venturini SW. Multiple random crack propagation using a boundary element formulation. Eng Fract Mech 2011;78:1077–90.